

# Fourier analysis of He 4471/Mg 4481 line profiles for separating rotational velocity and axial inclination in rapidly-rotating B-type stars\*

Y. Takeda<sup>1†</sup>, S. Kawanomoto,<sup>1</sup> and N. Ohishi<sup>1</sup>

<sup>1</sup>National Astronomical Observatory of Japan, 2-21-1 Osawa, Mitaka, Tokyo 181-8588, Japan

11 May 2018

## ABSTRACT

While the effect of rotation on spectral lines is complicated in rapidly-rotating stars because of the appreciable gravity-darkening effect differing from line to line, it is possible to make use of this line-dependent complexity to separately determine the equatorial rotation velocity ( $v_e$ ) and the inclination angle ( $i$ ) of rotational axis. Although line-widths of spectral lines were traditionally used for this aim, we tried in this study to apply the Fourier method, which utilizes the unambiguously determinable first-zero frequency ( $\sigma_1$ ) in the Fourier transform of line profile. Equipped with this technique, we analyzed the profiles of He I 4471 and Mg II 4481 lines of six rapidly-rotating ( $v_e \sin i \sim 150\text{--}300 \text{ km s}^{-1}$ ) late B-type stars, while comparing them with the theoretical profiles simulated on a grid of models computed for various combination of ( $v_e$ ,  $i$ ). According to our calculation,  $\sigma_1$  tends to be larger than the classical value for given  $v_e \sin i$ . This excess progressively grows with an increase in  $v_e$ , and is larger for the He line than the Mg line, which leads to  $\sigma_1^{\text{He}} > \sigma_1^{\text{Mg}}$ . It was shown that  $v_e$  and  $i$  are separately determinable from the intersection of two loci (sets of solutions reproducing the observed  $\sigma_1$  for each line) on the  $v_e$  vs.  $i$  plane. Yet, line profiles alone are not sufficient for their unique discrimination, for which photometric information (such as colors) needs to be simultaneously employed.

**Key words:** line: profiles – stars: atmospheres – stars: early-type – stars: rotation – stars: individual (17 Tau,  $\alpha$  Leo,  $\beta$  CMi,  $\eta$  Aqr,  $\eta$  Tau,  $\zeta$  Peg)

## 1 INTRODUCTION

In the widely used conventional treatment assuming the invariant line profile over the disk along with the circular-symmetric brightness distribution of limb-darkening (valid for slow rotators), the effect of stellar rotation on a spectral line is quite simple, which can be universally expressed by convolution of the rotational broadening function with the intrinsic profile (see, e.g., Gray 2005). In this case, the equatorial rotational velocity ( $v_e$ ) and the projection factor ( $\sin i$ , where  $i$  is the inclination angle of the rotation axis relative to the line of sight) always appears as both product ( $v_e \sin i$ ), and their separation is impossible.

Meanwhile, for the case of rapid rotators (e.g.,  $v_e \sim 100\text{--}400 \text{ km s}^{-1}$ ) commonly seen in early-type stars, such an approximation is no more valid in the practical sense, because

the gravity-darkening effect (i.e., temperature inhomogeneity on the surface) causes an appreciable variation in the strength and profile of spectral lines on the stellar disk, the extent of which is considerably line-dependent. Accordingly, the effect of rapid rotation on a spectral line is so complicated as to be treated only by detailed numerical calculations based on a properly designed gravity-darkened stellar model. In compensation for this complexity, however, separated determination of  $v_e$  and  $i$  may be possible by simultaneously analyzing the profiles of two or more lines of different temperature sensitivity.

Actually, several investigators challenged this delicate and difficult task of  $v_e$ – $i$  separation by carefully analyzing the spectral lines: Stoeckley (1968a) studied five rapidly rotating B and A-type stars by using He I 4471, Mg II 4481, and Ca II 3934 lines. Hutchings & Stoeckley (1977) examined the UV lines based on the Copernicus data (and also lines in the visual region) for 20 stars of mostly B-type. Rusaalepp (1982) computed the half-width of He I 4471 and Mg II 4481 lines for various model parameters and applied

\* Based on observations carried out at the Okayama Astronomical Observatory of National Astronomical Observatory of Japan.

† E-mail: takeda.yoichi@nao.ac.jp

to 19 early B-type stars. Stoeckley & Buscombe (1987) extended the previous work of Stoeckley (1968a) and analyzed the He I 4471 and Mg II 4481 lines of 19 rapidly-rotating B-type main-sequence stars, where they also tried to detect the degree of differential rotation (in addition to independent determination of  $v_e$  and  $i$ ).

Somewhat surprisingly, observational investigations of this kind seem to have been barely done since then over these 30 years, as far as we know,<sup>1</sup> When we review these old studies from the aspect of current knowledge, some points are noticed, which may have room for further improvement.

First, rather rough interpolation appears to have been adopted in the simulation of spectral line profiles in gravity-darkened stellar photospheres, which requires integrations of local spectra at many points over the visible stellar disk. Presumably, this is due to the limitation of computational capacity at the time. It may be possible nowadays to implement more realistic computations; e.g., by using our code developed for simulating the gravity-darkened spectrum of Vega (Takeda, Kawanomoto & Ohishi 2008).

Second, these previous studies employed “line widths” (mostly half-width at the half maximum of the line depth) for their analysis. However, precisely measuring the line width suffers practical difficulties for the relevant case of rapid rotators characterized by very wide and shallow profiles of merged line features, because it critically depends on the continuum level, for which exact determination is not easy. Given this situation, it occurred to us to apply the Fourier method, which utilizes the frequencies corresponding to the zero amplitude in the Fourier transform of a line profile, because these zero-frequencies are easily determinable from the amplitude vs. frequency diagram.

It appears that this Fourier approach has not been so popularly applied to early-type stars, which is presumably related to the problem involved with rapid rotators commonly seen in hot stars. As well known, its merit for rotational velocity study is especially manifest when the emergent line flux profile ( $F_\lambda$ ) is expressed by convolution of the intrinsic stellar flux profile ( $T_\lambda$ ) and the rotational broadening function ( $G_\lambda$ ). That is, the value of  $v_e \sin i$  can be determined directly from the zeros of observed  $f(\sigma)$  (transform of  $F_\lambda$ ) without any necessity of deconvolving  $T_\lambda$ , because the zeros of  $g(\sigma)$  (transform of  $G_\lambda$ ) are automatically inherited to  $f(\sigma)$  in the Fourier space where “convolution” in the wavelength space simply turns into “multiplication.” It should be remarked, however, that this conventional treatment using the classical rotational broadening function [cf. Eq. (18.14) in Gray (2005)] is based on the assumptions that (i) the line profile has the same shape at any point on the stellar disk and (ii) the brightness distribution on the stellar disk is circularly symmetric to be represented by a simple limb-darkening law, which are evidently not valid any more for rapid rotators showing considerable gravity darkening as well as rotational distortion. Actually, we know only a few trials of Fourier analysis for  $v_e \sin i$  determination with the

classical rotational broadening function in the field of hot stars; e.g., Simón-Díaz & Herrero (2007) for OB stars or Díaz et al. (2011) for A-type stars. If line profiles of rapidly rotating stars are to be adequately analyzed, special considerations had to be made toward derivation of specific rotational broadening function, such as done by several investigators (cf. Stoeckley & Mihalas 1973; Collins & Truax 1995; Levenhagen 2014).

Given this situation, we decided to carry out a feasibility study to examine whether it is possible to separately determine  $v_e$  and  $i$  based on the Fourier analysis of line profiles for selected six rapidly-rotating late B-type stars, since such a trial seems to have been barely made to our knowledge.<sup>2</sup> For this purpose, we calculated a set of theoretical profiles on a grid of gravity-darkened models for various combinations of ( $v_e$ ,  $i$ ). Here, we focus only on He I 4471 and Mg II 4481 lines, which are suitable for the present aim and actually have been widely used so far. Our strategy is to compare the zeros in the Fourier transforms of the observed and the numerically simulated profiles directly to each other. In this sense, our analysis (except for the first preparatory analysis following the conventional procedure) is irrelevant to the concept of rotational broadening function (whichever classical or special) used to model the line profile by convolution. Yet, we also examine how the zeros in the Fourier transforms of the realistically computed line profiles of rapid rotators are compared with those of the classical rotational broadening, which would be worthwhile for evaluating the accuracies of apparent  $v_e \sin i$  values derived from the conventional treatment.

The remainder of this paper is organized as follows. Our observational data of six target stars are described in Sect. 2. In Sect. 3 are presented the results of our preparatory analysis following the standard procedure (parameter determination from colors, examination of positions on the HR diagram, spectrum-fitting analysis by using the classical rotational broadening function, evaluation of equivalent widths, etc.). Profile simulations of He 4471 and Mg 4481 lines based on gravity-darkened models and Fourier transform calculations of observed as well as theoretical profiles are explained in Sect. 4. Sect. 5 is the discussion section, where the characteristics of first-zero locations are examined, and we try separate determinations of  $v_e$  and  $i$  by comparing the observed first-zero frequency with the theoretical grid. The summary of this investigation is given in Sect. 6.

<sup>2</sup> We note that several researchers have recently conducted sophisticated modeling of theoretical line profiles for rapidly-rotating B-type stars under the effect of gravity darkening, and also investigated the possibility of Fourier transform method for extracting in-depth information of stellar rotation such as the nature of differential rotation (e.g., Domiciano de Souza et al. 2004, Zorec et al. 2011, 2017). However, these studies placed emphasis on simulations of model profiles with particular intention of applying to Be stars based on combined interferometric and spectroscopic observations, which are thus somewhat different from the topic under question.

<sup>1</sup> Vinicius, Townsend & Leister (2007) reported their preliminary results for the rotational inclination of five early B-type (Be) stars determined from the strengths (not the widths) of various spectral lines, though they do not appear to have published the details of their analysis.

## 2 OBSERVATIONAL DATA

As the targets of this study, we selected 6 apparently bright ( $V \sim 1\text{--}4$ ) late B-type stars (spectral type of B6–B9 and luminosity classes of III–V; cf. Table 1), all of which are known to be rapid rotators with  $v_e \sin i \sim 100\text{--}300 \text{ km s}^{-1}$  (e.g., Abt, Levato & Grosso 2002).

Note that 3 stars ( $\eta$  Tau,  $\beta$  CMi, 17 Tau) out of these 6 program stars are classified as classical Be stars according to Jaschek & Egret’s (1982) catalogue. Actually, we can confirm the existence of appreciable emission component in H $\alpha$  in the spectra of these 3 stars (especially for  $\eta$  Tau and  $\beta$  CMi).<sup>3</sup> Accordingly, we should keep in mind a possibility that the spectra may be contaminated by circumstellar Be disk for these stars. However, we consider that such an effect (even if any exists) is presumably not significant for the He 4471/Mg 4481 lines, because no particular anomaly is seen in the strengths of these He and Mg lines for these Be stars as compared to those for other normal B stars (cf. Sect. 3.2).

The observations were carried out on 2006 November 1 ( $\beta$  CMi,  $\eta$  Tau), 2 ( $\zeta$  Peg), and 4 (17 Tau,  $\alpha$  Leo, and  $\eta$  Aqr) by using the High-Dispersion Echelle Spectrograph (HIDES; Izumiura 1999) at the coudé focus of the 188 cm reflector of Okayama Astrophysical Observatory (OAO). Equipped with a 4K $\times$ 2K CCD detector at the camera focus, the HIDES spectrograph enabled us to obtain an echellogram covering a wavelength range of 3860–4630 Å with a resolving power of  $R \sim 70000$  (case for the normal slit width of 200  $\mu\text{m}$ ) in the mode of blue cross-disperser. The total exposure time for each star ranged from 6 min to 100 min depending on the stellar brightness or the weather condition.

The reduction of the spectra (bias subtraction, flat-fielding, scattered-light subtraction, spectrum extraction, wavelength calibration, co-addition of frames to increase the S/N ratio, and continuum normalization) was performed by using the “echelle” package of the software IRAF<sup>4</sup> in a standard manner. The S/N ratios of the finally resulting spectra turned out to be sufficiently high for the present purpose ( $\gtrsim 500$  for most stars at the 4450–4500 Å region).

## 3 CONVENTIONAL MODEL ATMOSPHERE ANALYSIS

Before going into the Fourier analysis of spectral line profiles, we first conducted a preparatory study following the conventional manner, in order to grasp the basic characteristics of program stars.

### 3.1 Stellar parameters

The effective temperature ( $T_{\text{eff}}$ ) and the surface gravity ( $\log g$ ) of each star were determined from the colors of Strömgren’s  $uvby\beta$  photometric system with the help of

Napiwotzki, Schönberner, and Wenske’s (1993)  $uvby\beta$  program<sup>5</sup>, where the observational data of  $b - y$ ,  $c_1$ ,  $m_1$ , and  $\beta$  were taken from Hauck and Mermilliod (1998) via the SIMBAD database. The resulting  $T_{\text{eff}}$  and  $\log g$  are summarized in Table 1.

We also estimated the luminosity ( $L$ ) of these stars by using the Hipparcos parallaxes (ESA 1997) along with the extinction correction (Arenou, Grenon & Gomez 1992) and bolometric correction (Flower 1996), as done by Takeda et al. (2010). These  $\log L$  values are plotted against  $\log T_{\text{eff}}$  in Fig. 1, where Ekström et al.’s (2012) theoretical evolutionary tracks for both rotating and non-rotating models are also depicted. We can see from this figure that the masses of our sample stars are in the range between  $\sim 3 M_{\odot}$  and  $\sim 5 M_{\odot}$ . By comparing  $M$  and  $\log g$ , we find that the radius values are  $R \sim 3\text{--}6 R_{\odot}$  for most stars (excepting  $\eta$  Tau, for which  $R \sim 10 R_{\odot}$ ).

### 3.2 Synthetic spectrum fitting

Then, spectrum-synthesis analysis was carried out for the He 4471+Mg 4481 line feature in the same manner as described in Sect. 4.2 of Takeda et al. (2010). That is, while applying the optimization algorithm described in Takeda (1995), we determined the solutions of  $A(\text{He})$  (He abundance),  $A(\text{Mg})$  (Mg abundance),  $v_e \sin i$  (projected rotational velocity), and  $\Delta\lambda$  (radial velocity shift) accomplishing the best fit between the theoretical and observed spectra, where the rotational broadening was treated by convolving the intrinsic flux profile with the rotational broadening function (limb-darkening coefficient of  $\epsilon = 0.5$ ). Neither the instrumental broadening nor the macroturbulence broadening was taken into account, which are negligible compared to the rotational broadening.

The model atmosphere for each star used for this analysis was constructed by two-dimensionally interpolating Kurucz’s (1993) ATLAS9 model grid (solar-metallicity models) in terms of  $T_{\text{eff}}$  and  $\log g$ . Regarding the He I 4471 line (multiplet No. 14;  $\chi_{\text{low}} = 20.96 \text{ eV}$ ), we adopted the total  $gf$  value (summed over components) of 1.13 (cf. Table 2b of Takeda 1994) and the opacity profile (with forbidden components) broadened by Stark damping was treated according to Barnard, Cooper & Smith (1974). As to the atomic line data for Mg II 4481 (Multiplet No. 4;  $\chi_{\text{low}} = 8.86 \text{ eV}$ ), we consulted the VALD database (Ryabchikova et al. 2015), which gives  $\log gf = +0.740$ ,  $-0.560$ , and  $+0.590$  for the components at 4481.126, 4481.150, and 4481.325 Å, respectively. The microturbulent velocity was fixed at  $2 \text{ km s}^{-1}$ .

We assumed LTE throughout this study. The non-LTE effect for the He 4471 and Mg 4481 lines is not likely to be important as far as late-B stars are concerned, even though it should act in the direction of intensifying the strengths of lines for both cases. According to Auer & Mihalas (1973), the non-LTE increase in the equivalent width for the He 4471 line is only  $\sim 5\%$  for the model of  $T_{\text{eff}} = 15000 \text{ K}$  and  $\log g = 4.0$ , which becomes even less significant as  $T_{\text{eff}}$  is lowered. Regarding the Mg 4481 line, the non-LTE abundance correction for the A0V star Vega ( $T_{\text{eff}} \simeq 9500 \text{ K}$  and  $\log g \simeq 4.0$ ) was reported to be  $\sim -0.1 \text{ dex}$  (Gigas 1988) or

<sup>3</sup> See, e.g., the spectral collection of Be stars available at <http://www.astrosurf.com/buil/us/becat.htm>.

<sup>4</sup> IRAF is distributed by the National Optical Astronomy Observatories, which is operated by the Association of Universities for Research in Astronomy, Inc. under cooperative agreement with the National Science Foundation.

<sup>5</sup> (<http://www.astro.le.ac.uk/~rn38/uvbybeta.html>).

$\sim -0.2$  dex (Przybilla et al. 2001), which corresponds to a non-LTE intensification of equivalent width ( $W \sim 300$  mÅ) by  $\sim 5$ –10%. Since this non-LTE effect decreases with an increase of  $T_{\text{eff}}$  (i.e., with a decrease in  $W$ ), it would be insignificant in the regime of late B-type stars, which is also supported by Mihalas’s (1972) calculation for mid- through early-B stars.

How the best-fit theoretical spectrum (corresponding to the converged parameter solutions) matches the observed one for each star is shown in Fig. 2. It is instructive to note that an apparently satisfactory fit can be achieved even by such a classical modeling using a plane-parallel model atmosphere for given  $T_{\text{eff}}$  and  $\log g$ , if  $A(\text{He})$ ,  $A(\text{Mg})$ ,  $v_e \sin i$ , and  $\Delta\lambda$  are adequately adjusted. This means that separate determination of  $v_e$  and  $i$  is a very delicate matter, which is hardly discernible by simply eye-inspecting the line profiles. We also computed the equivalent widths  $W(\text{He } 4471)$  and  $W(\text{Mg } 4481)$  inversely from the converged solutions of  $A(\text{He})$  and  $A(\text{Mg})$  as done in Takeda et al. (2010; see Sect. 4.3 therein). The resulting values of  $v_e \sin i$ ,  $W(\text{He})$ , and  $W(\text{Mg})$  are presented in Table 1. Such derived  $W$  values are plotted against  $T_{\text{eff}}$  in Fig. 3, where the theoretical relations are also depicted. We can see from this figure that the trend of  $W$  with a change in  $T_{\text{eff}}$  is roughly in agreement with the theoretical prediction.

## 4 FOURIER ANALYSIS OF SPECTRAL LINES

### 4.1 Transform of line profiles

On both sides of a line for given flux spectrum  $F(\lambda)$ , we select two reference wavelengths ( $\lambda_1$  and  $\lambda_2$ ), at which we may regard  $F(\lambda_1)$  and  $F(\lambda_2)$  as the level of pseudo-continuum. The normalized line depth  $R(\lambda)$  is defined within a limited range of  $\lambda_1 \leq \lambda \leq \lambda_2$  as

$$R(\lambda) \equiv 1 - F(\lambda)/F_c \quad (1)$$

(while  $R(\lambda) \equiv 0$  outside of this range), where  $F_c$  is the linear-interpolation of  $F(\lambda_1)$  and  $F(\lambda_2)$  in terms of  $\lambda$ :

$$F_c \equiv \frac{\lambda_2 - \lambda}{\lambda_2 - \lambda_1} F(\lambda_1) + \frac{\lambda - \lambda_1}{\lambda_2 - \lambda_1} F(\lambda_2). \quad (2)$$

The Fourier transform of  $R(\lambda)$  is expressed as (see, e.g., Gray 2005)

$$f(\sigma) \equiv \int_{-\infty}^{\infty} R(\lambda) \exp(2\pi i \sigma \lambda) d\lambda. \quad (3)$$

Regarding the choice of reference points in the observed spectrum, we paid attention to the critical wavelength ( $\lambda^*$ ) of highest flux level between the He 4471 and Mg 4481 lines (around  $\sim 4476$ – $4478$  Å), and equated as  $\lambda_2^{\text{He}} = \lambda_1^{\text{Mg}} = \lambda^*$ , from which  $\lambda_1^{\text{He}}$  and  $\lambda_2^{\text{Mg}}$  were so chosen as to be symmetric relative to the line wavelength. The relevant reference wavelengths ( $\lambda_1^{\text{He}}$ ,  $\lambda^*$ , and  $\lambda_2^{\text{Mg}}$ ) we adopted for each star are marked by green crosses in Fig. 2.

Fig. 4 illustrates the amplitudes of the computed Fourier transforms  $|f(\sigma)|$  for the observed profiles of He 4471 and Mg 4481 lines as functions of  $\sigma$  for each star. We can see that the critical frequency ( $\sigma_1$ ) corresponding to the first-zero of  $f(\sigma)$  is clearly recognized by the cuspy feature and easily determinable. The measured values of  $\sigma_1$  are given in Table 1.

### 4.2 Spectrum simulation with gravity-darkened models

Regarding the modeling of rotating stars with gravity darkening, we adopt the same assumption and parameterization described in Sect. 2.1 and 2.2 of Takeda, Kawanomoto & Ohishi (2008). Our model (Roche model with the assumption of rigid rotation) is characterized by stellar mass ( $M$ ), polar radius ( $R_p$ ), polar effective temperature ( $T_{\text{eff,p}}$ ), and equatorial rotational velocity ( $v_e$ ), which suffice to express the surface quantities [ $r(\theta)$ ,  $T_{\text{eff}}(\theta)$ ,  $g(\theta)$ ,  $v(\theta)$ ] as functions of  $\theta$  (colatitude angle). Regarding the exponent  $\beta$  in the relation  $T_{\text{eff}} \propto g^\beta$  determining the degree of gravity darkening, we used the  $T_{\text{eff}}$ -dependent analytical formula [ $\beta = f(T_{\text{eff}})$ ]<sup>6</sup> based on Fig. 5 of Claret (1998) as done in Takeda, Kawanomoto & Ohishi (2008; cf. footnote 2 therein). Since different model atmosphere corresponding to the local ( $T_{\text{eff}}$ ,  $g$ ) is defined at each point on the surface, we can compute the flux profile to be observed by an external observer by integrating the emergent intensity profile over the visible disk for any inclination angle ( $i$ ) of the rotational axis, while using the program CALSPEC (see Sect. 4.1 in Takeda, Kawanomoto & Ohishi 2008). As such, in order to compute a spectrum, it is necessary to specify five parameters:  $M$ ,  $R_p$ ,  $T_{\text{eff,p}}$ ,  $v_e$ , and  $i$ .

Given that our main purpose is to examine the feasibility of spectroscopically separating  $v_e$  and  $i$ , it is requisite to accomplish a sufficient number of grid regarding these two parameters, while changing other parameters is not necessarily important as long as their effects on line profiles are comparatively insignificant. Therefore, considering the ranges of  $M$  and  $R$  estimated in Sect. 3.1, we assume  $M = 4.0 M_\odot$  and  $R = 4.0 R_\odot$  as fixed. Since the photometric  $T_{\text{eff}}$  derived from colors ( $\sim 11000$ – $13000$  K; cf. Table 1) should reflect the mean  $T_{\text{eff}}$  averaged over the visible disk, the polar  $T_{\text{eff,p}}$  must be appreciably larger, though the difference intricately depends upon  $v_e$  and  $i$ . We tentatively assume two  $T_{\text{eff,p}}$  cases of 12000 K and 15000 K, hoping that they sufficiently cover the temperature range of 6 program stars. Accordingly, adopting the same line data and the assumptions as described in Sect. 3.2 along with the solar abundances of He and Mg, we computed 120 ( $= 6 \times 10 \times 2$ ) spectra of He 4471+Mg 4481 line feature, corresponding to combinations of 6  $v_e$  values (100, 150, 200, 250, 300, and 350 km<sup>-1</sup>), 10  $i$  values (0, 10, 20, 30, 40, 50, 60, 70, 80, and 90°), and 2  $T_{\text{eff,p}}$  values (12000 K and 15000 K). The parameters of these models are listed in Table 2, where the corresponding values of  $\langle T_{\text{eff}} \rangle$  (intensity-weighted average of  $T_{\text{eff}}$  over the

<sup>6</sup> According to this formula,  $\beta$  becomes equal to von Zeipel’s value of 0.25 at the higher  $T_{\text{eff}}$  region of  $\log T_{\text{eff}} \geq 0.9$  ( $T_{\text{eff}} \geq 7943$  K). Since most of our models fall in this  $T_{\text{eff}}$  range (though the minimum  $T_{\text{eff}}$  is 7204 K in the exceptional case), we may say that the simple von Zeipel’s law was adopted for almost all models. However, we should keep in mind a possibility that actual  $\beta$  may deviate from the von Zeipel value (0.25) even at such a higher  $T_{\text{eff}}$  range where the radiative equilibrium holds in the stellar envelope. That is, according to Espinosa Lara & Rieutord’s (2011) calculation,  $\beta$  is a function of rotational flattening in the sense that  $\beta$  progressively decrease from  $\sim 0.25$  (no rotation) to  $\sim 0.15$  (near to the rotational break-up limit). If this is really the case, the simple application of  $\beta = 0.25$  to rapidly rotating stars may lead to an overestimation of gravity darkening.

visible disk) are also presented. Several selected examples of the resulting spectra are depicted in Fig. 5.

The wavelengths of the reference pseudo-continuum, necessary for reducing the normalized profile, were defined in almost the same way as in Sect. 4.1: Having found the critical wavelength  $\lambda^*$  corresponding to the maximum level between these two lines, we set  $[\lambda_1^{\text{He}}, \lambda_2^{\text{He}}] = [4471 - (\lambda^* - 4471), \lambda^*]$  and  $[\lambda_1^{\text{Mg}}, \lambda_2^{\text{Mg}}] = [\lambda^*, 4481 + (4481 - \lambda^*)]$ . The Fourier transforms were then calculated for the resulting  $R(\lambda)$  profiles of He 4471 and Mg 4481 lines. Fig. 6 illustrates the behaviors of  $|f(\sigma)|$  as function of  $\sigma$  for the same selected cases as in Fig. 5. The first-zero frequencies ( $\sigma_1$ ) measured from the computed transforms are presented in Table 2.

## 5 DISCUSSION

### 5.1 Characteristics of first-zero frequencies

We first discuss the trend of theoretical  $\sigma_1$  modeled in Sect. 4.2. Since this quantity is expressed as  $\sigma_1 = 0.660/(\lambda v_e \sin i/c)$  in the classical approximation, the projected rotational velocity (or the line-width for the case of rotation-dominated broadening) plays the most significant role, though its precise value is affected also by the profile shape. The resulting values of  $\sigma_1$  corresponding to the theoretical line profiles simulated on the gravity-darkened models are plotted against  $v_e \sin i$  in Fig. 7, where the classical  $\sigma_1$  vs.  $v_e \sin i$  relation is depicted by a slanted solid line and the observed  $\sigma_1$  values for 6 stars are indicated by horizontal dashed lines.

We can see from this figure that the  $\sigma_1$  values of the simulated spectra closely follow the classical relation (i.e., inversely proportional to  $v_e \sin i$ ), as long as  $v_e \sin i$  is small (e.g., up to several tens  $\text{km s}^{-1}$ ),  $\sigma_1$ , though appreciable deviations ( $\sigma_1$  tends to be larger than the classical value) reflecting the gravity-darkening effect begin to be recognized as  $v_e \sin i$  becomes larger. A closer inspection of the figure reveals that (i) the extent of deviation is essentially determined by  $v_e$ , (ii) this discrepancy is more manifest for He 4471 than for Mg 4481, and (iii) no significant difference exists regarding the trend of  $\sigma_1$  between the  $T_{\text{eff,p}} = 12000$  K and 15000 K cases (though the deviation being slightly larger for the former).

The fact that  $\sigma_1$  tends to be in excess of the classical value is reasonably explained by considering the physical effect caused by gravity darkening. In the rotationally-broadened spectral lines, the line width is mainly determined by maximum Doppler velocity caused by rotation (i.e.,  $v_e \sin i$ ), to which the low-latitude region near to the equator makes most significant contribution because the absolute rotational velocity is largest there. In the case of rapid rotators with large  $v_e$ , these equatorial regions are considerably darkened and thus their contribution to line broadening becomes lessened. Accordingly, the width becomes narrower compared to the classical case, which eventually shifts  $\sigma_1$  to a larger value. Moreover, this effect is further amplified for the case of He 4471, because the strength of this line quickly drops as  $T_{\text{eff}}$  is lowered (cf. Fig. 3). Consequently, the inequality relation  $\sigma_1^{\text{He}} > \sigma_1^{\text{Mg}}$  holds for rapid-rotator models, which is actually observed in our program stars (cf. Fig. 4).

Another important implication read from Fig. 7 is that  $\sigma_1$  tends to be stabilized at the high-rotation limit ( $\gtrsim 300 \text{ km s}^{-1}$ ), in the sense that  $\sigma_1$  does not effectively decrease (or line width does not effectively increase) any more no matter how the rotational velocity is increased, which is because two effects (increase of rotation and enhanced gravity darkening) on the width counteract with each other and tend to be cancelled. Actually, this effect was first pointed out by Stoeckley (1968b) and also confirmed by Townsend, Owocki & Howarth (2004); i.e., rotational velocities of rapidly-rotating stars (especially those close to the limit) may be significantly underestimated if simply determined from the apparent line widths.

### 5.2 Separation of rotation and inclination

Now that we have theoretical  $\sigma_1$  values as functions of  $v_e$  and  $i$  for He 4471 as well as Mg 4481 lines, we can compare them with the observed  $\sigma_1$ . Then, a possible set of  $(v_e, i)$  solutions is expressed as a locus on the  $v_e$  vs.  $i$  plane by solving the equation  $\sigma_1^{\text{th}}(v_e, i) = \sigma_1^{\text{obs}}$  for each line, from which  $(v_e, i)$  may be established from the intersection of two loci on the plane. Such constructed loci (displayed in Fig. 8), and the estimation of  $(v_e, i)$  values (summarized in Table 1) are discussed below star by star.

#### 5.2.1 $\zeta$ Peg

Fig. 8a and Fig. 8a' represent the characteristic difficulty involved with this analysis. Since the loci derived for He and Mg lines are rather similar in shape, the intersection is not clearly defined. To our embarrassment, this similarity brings about a marked difference of  $(v_e, i)$  solution depending on  $T_{\text{eff,p}}$ , despite that  $\sigma_1$  is not so sensitive to it (cf. Sect. 4.2). That is, ( $\sim 150$ – $200 \text{ km s}^{-1}$ ,  $\sim 50$ – $60^\circ$ ) for 12000 K and ( $\sim 250$ – $300 \text{ km s}^{-1}$ ,  $\sim 30$ – $40^\circ$ ) for 15000 K. Fortunately, however, the former (more equator-on-like slower rotation) and the latter (more pole-on-like faster rotation) yield distinctly different  $\langle T_{\text{eff}} \rangle$ ; i.e.,  $\sim 11200$ – $11500$  K and  $\sim 13000$ – $13700$  K according to Table 2. Comparing these with  $T_{\text{eff}}^{\text{color}}$  of  $\sim 12700$  K, we can guess that the actual solution would be almost the intermediate between these two as ( $\sim 200$ – $250 \text{ km s}^{-1}$ ,  $\sim 40$ – $50^\circ$ ). Stoeckley & Buscombe (1987) derived [ $195$  ( $158$ – $246$ )  $\text{km s}^{-1}$ ,  $54$  ( $40$ – $90^\circ$ )] for this star, nearly consistent with our result.

#### 5.2.2 $\eta$ Aqr

This star has the largest  $v_e \sin i$  of  $\sim 290 \text{ km s}^{-1}$  among our 6 sample stars. Unfortunately, we were unable find the solution for this star, because the  $\sigma_1^{\text{obs}}$  values (0.172 for He and 0.153 for Mg) are too small to be covered by the grid of  $\sigma_1^{\text{th}}$  (see Fig. 7). The reason for this incompatibility is not clear. It might be possible that the physical condition can not be adequately described by our modeling for such case of very rapid rotator. Alternatively, there might be systematic errors in the measurement of  $\sigma_1$  for such case of especially large  $v_e \sin i$ , because He and Mg lines tend to somewhat merge in-between (Fig. 2). In this context, the ambiguity in the measurement of  $\sigma_1^{\text{He}}$  would be larger than  $\sigma_1^{\text{Mg}}$ , because the cuspy feature near to the zero amplitude is less sharp

for the former than the latter (cf. Fig. 4b). As a test, we increased the original  $\sigma_1^{\text{He}}$  arbitrarily by 10% ( $0.172 \rightarrow 0.189$ ) and made a retry. In this case, we could find a solution for the  $T_{\text{eff,p}} = 15000$  K case (but failed again for the 12000 K case) as shown in Fig. 8b', which suggests ( $\sim 300$  km s $^{-1}$ ,  $\sim 80$ – $90^\circ$ ). In any event, we may conclude that this star is a very rapidly rotating star ( $v_e \sim 300$  km s $^{-1}$  or even somewhat larger) seen nearly equator-on. In such cases, solution search becomes especially difficult, because  $i = 90^\circ$  is a singularity point, in the sense that it can not be encompassed by  $i$  values of the grid. As such, the feasibility of establishing the solution is quite vulnerable to errors in  $\sigma_1$  or modeling inadequacies.

### 5.2.3 $\eta$ Tau

The  $(v_e, i)$  for this star appears to be comparatively easier to embrace. Since the intersection of He and Mg loci lies at ( $\sim 300$  km s $^{-1}$ ,  $\sim 35^\circ$ ) for  $T_{\text{eff,p}} = 12000$  K (Fig. 8c) and at ( $\sim 350$  km s $^{-1}$ ,  $\sim 30^\circ$ ) for  $T_{\text{eff,p}} = 15000$  K (Fig. 8c') and not much different from each other, we may regard that this star is a very rapid rotator with  $v_e \sim 300$ – $350$  km s $^{-1}$  seen from a rather low inclination angle ( $i \sim 30$ – $35^\circ$ ).

### 5.2.4 $\beta$ CMi

We could not find a reasonable solution for this star. First,  $\sigma_1^{\text{He}}$  is so small (as is the case for  $\eta$  Aqr) and no He-locus exists for  $T_{\text{eff,p}} = 12000$  K (Fig. 8d). Meanwhile, no clear intersection point can be defined for the  $T_{\text{eff,p}} = 15000$  K case (Fig. 8d'). Although we may roughly speculate from these figures  $v_e \sim 250$ – $300$  km s $^{-1}$  and  $i \sim 60$ – $80^\circ$  as the possible ranges (i.e., rather high inclination angle), any conclusion should be withheld. On the other hand, Stoeckley (1968a) reported (as a tentative conclusion) the aspect angle of this star to be  $i \sim 30$ – $50^\circ$ .

### 5.2.5 $\alpha$ Leo

Almost the same situation holds for this star as the case of  $\eta$  Aqr, since the  $\sigma_1$  values are indiscernibly similar to each other (cf. Fig. 7), which means that no solution exists because  $\sigma_1$  is outside of the range of the grid. Again, we increased  $\sigma_1^{\text{He}}$  by 10% ( $0.172 \rightarrow 0.189$ ), as a trial and searched for the  $(v_e, i)$  solution. Naturally, the results are essentially the same as the case for  $\eta$  Aqr (compare Fig. 8e' with Fig. 8b'), suggesting ( $\sim 300$  km s $^{-1}$ ,  $\sim 80$ – $90^\circ$ ) as a rough estimate. We may thus at least state that  $\alpha$  Leo is a very rapidly-rotating star seen nearly equator-on. This is consistent with the previous determinations: ( $300$  km s $^{-1}$ ,  $90^\circ$ ) estimated by Hutchings & Stoeckley (1977) from the widths of UV lines, [ $285$  ( $270$ – $309$ ) km s $^{-1}$ ,  $90$  ( $67$ – $90$ ) $^\circ$ ] determined by Stoeckley & Buscombe (1987) from the widths of He 4471 and Mg 4481 lines, and [ $317 \pm 3$  km s $^{-1}$ ,  $75$ – $90^\circ$ ] concluded by McAlister et al. (2005) based on interferometric observations.

### 5.2.6 $17$ Tau

The behavior of loci on the  $v_e$  vs.  $i$  plane for this star is similar to the case of  $\zeta$  Peg. The intersection of He and Mg

loci depends on  $T_{\text{eff,p}}$  as ( $\sim 200$  km s $^{-1}$ ,  $\sim 60^\circ$ ) for 12000 K and ( $\sim 300$  km s $^{-1}$ ,  $\sim 30$ – $40^\circ$ ) for 15000 K, each of which correspond to  $\langle T_{\text{eff}} \rangle$  of  $\sim 11000$  K and  $\sim 13000$  K according to Table 2. Considering that  $T_{\text{eff}}^{\text{color}}$  is  $\sim 12700$  K, we conclude that the latter solution is relevant, which means that this star is very rapidly-rotating with  $v_e \sim 300$  km s $^{-1}$  and seen with a rather low aspect angle ( $i \sim 30$ – $40^\circ$ ).

### 5.2.7 Comparison with Zorec et al.'s (2016) results

Zorec et al. (2016) recently studied the rotational velocity distribution of a large sample of 233 Be stars. They also separated rotation and inclination for each star by comparing the observed stellar parameters affected by rotation (effective temperature, surface gravity, luminosity, projected rotational velocity) with extensive theoretical calculations based on gravity-darkened stellar models (cf. Appendix E therein). Since three of our targets are included in their sample, it is interesting to compare our profile-based results of axial inclination with their determinations. Comparing their  $i$  values ( $62 \pm 15^\circ$ ,  $66 \pm 16^\circ$ , and  $45 \pm 11^\circ$  for  $\eta$  Tau,  $\beta$  CMi, and  $17$  Tau, respectively) with our results presented in Table 1 ( $\sim 30$ – $35^\circ$ ,  $\sim 60$ – $80^\circ$ , and  $\sim 30$ – $40^\circ$ ), we notice an appreciable disagreement for  $\eta$  Tau, although a reasonable consistency is seen for  $\beta$  CMi and  $17$  Tau. This discrepancy for  $\eta$  Tau may be attributed to the fact that this is an exceptional case of evolved subgiant ( $R \sim 10R_\odot$ ) among our sample (cf. Sect. 3.2). Our result for this star would be less reliable, because theoretical calculations corresponding to main-sequence B stars ( $R = 4R_\odot$ ) were applied to it like others.

## 6 SUMMARY AND CONCLUSION

It is known that the gravity-darkening effect causes an appreciable latitudinal inhomogeneity on the surface of a rapidly-rotating star; i.e., lower  $T_{\text{eff}}$  as well as  $g$  at lower latitude (in short, cool/dark equator and hot/bright pole). Owing to this effect, the impact of rotation on the shape of spectral lines is complicated and different from line to line, and the simple classical treatment (convolution of the intrinsic profile with the rotational broadening function determined by  $v_e \sin i$ ) is no more valid.

From the converse point of view, it is possible to make advantage of this line-dependent complexity to separately determine the equatorial rotational velocity ( $v_e$ ) and the inclination angle ( $i$ ) of rotational axis, which is impossible within the framework of the conventional approximation. Although several investigators challenged this task several decades ago, those old studies appear rather outdated as viewed from the present-day standard, especially in terms of their policy of simply invoking line-widths and seemingly insufficient accuracy in simulating line-profiles.

We thus tried to examine in this study whether the Fourier method, which is a comparatively modern technique utilizing the unambiguously determinable first-zero frequency of the Fourier transform of a line profile, is applicable to this problem of spectroscopically separating  $v_e$  and  $i$ . Conveniently, since we already have a computer code of simulating line profiles for a rapidly-rotating star with distorted surface of inhomogeneous brightness, we can make

use of it. As to the lines to be analyzed, we chose He I 4471 and Mg II 4481 lines, which have been often used for this purpose because they are strong and have markedly different temperature sensitivity.

Toward this aim, six rapidly-rotating late B-type stars ( $\zeta$  Peg,  $\eta$  Aqr,  $\eta$  Tau,  $\beta$  CMi,  $\alpha$  Leo, 17 Tau) were selected as our targets, for which high-dispersion spectra of sufficient quality are available. We first evaluated  $T_{\text{eff}}$  and  $\log g$  from  $uvby\beta$  colors, and then carried out a conventional spectrum-fitting analysis on the He 4471+Mg 4481 line feature based on plane-parallel model atmospheres to estimate  $v_e \sin i$  and the equivalent widths of two lines.

The theoretical line profiles of gravity-darkened rapid rotators were simulated for a grid of models for various combinations of  $v_e$  (100–350 km s<sup>-1</sup>) and  $i$  (0–90°), while typical values were assumed for other parameters ( $T_{\text{eff,p}} = 12000$  K and 15000 K,  $M_p = 4.0 M_\odot$ ,  $R_p = 4.0 R_\odot$ ). We then computed their Fourier transforms and measured the frequencies corresponding to the first zero ( $\sigma_1$ ).

These modeled  $\sigma_1$  values revealed the characteristic trends, reflecting the gravity-darkening effect and the different temperature susceptibility of these lines. (i) They tend to be in excess of the classical value  $\sigma_1^{\text{cl}} = 0.660/(\lambda v_e \sin i/c)$  when compared at a given  $v_e \sin i$ , and this difference progressively grows with an increase in  $v_e$ . (ii) The amount of this excess is larger for He 4471 than for Mg 4481, resulting in an inequality relation  $\sigma_1^{\text{He}} > \sigma_1^{\text{Mg}}$ .

Then, by comparing the  $\sigma_1$  of the observed profile with the theoretical grid of  $\sigma_1(v_e, i)$  for each of the He 4471 and Mg 4481 line, we can define two loci on the  $v_e$  vs.  $i$  plane, from which  $(v_e, i)$  may be separately determined from their intersection. We tried this solution search for 6 program stars, and confirmed that the intersection point is measurable, except for the difficult case of largest  $v_e \sin i$  ( $\eta$  Aqr and  $\alpha$  Leo; equator-on case with considerably large  $v_e$ ). However, since the position of this intersection tends to depend upon  $T_{\text{eff,p}}$ , its adequate specification was often necessarily, for which we compared  $\langle T_{\text{eff}} \rangle$  of the theoretical grid with  $T_{\text{eff}}^{\text{color}}$ . That is, line profiles alone are not sufficient but photometric information needs to be simultaneously employed.

To conclude, we could show in this investigation that the Fourier method using the first-zero frequencies in the transforms of line profiles is effectively applicable to separation of  $v_e$  and  $i$ . Although this approach is not essentially different from the traditional method using line widths, it has a merit that characteristic zero point of the transform is comparatively easier to measure even for the case of rapid rotators.

Yet, such a rough feasibility study as attempted in this paper still has room for further improvements. We enumerate below several issues to be considered in the future.

- Although we employed only He 4471 and Mg 4481 lines, simultaneously using more lines of different parameter sensitivity would surely improve the reliability of the solutions.
- Our adopted grid of theoretical gravity-darkened models was rather rough, especially in terms of the parameters other than  $v_e$  and  $i$  (i.e.,  $T_{\text{eff,p}}$ ,  $R_p$ ), for which much finer mesh would be required.
- Since the assumption of rigid rotation is not necessarily guaranteed, additional parameter describing the degree of differential rotation would desirably be included.

- Similarly, the possibility of rotation-dependence in the exponent  $\beta$  (see footnote 6), which determines the degree of gravity darkening, should be seriously investigated.

- In our Fourier analysis of line profiles, we made use of only  $\sigma_1$ , which is nothing but one of the various quantities characterizing the Fourier transform. It may be possible to utilize other observables such as the second-zero frequency or the amplitude of the side lobe.

When advanced analysis has been carried out by adequately taking account of these points, more realistic and trustworthy results would be expected.

## ACKNOWLEDGMENTS

This research has made use of the SIMBAD database, operated by CDS, Strasbourg, France. This work has also made use of the VALD database, operated at Uppsala University, the Institute of Astronomy RAS in Moscow, and the University of Vienna.

## REFERENCES

- Abt, H. A., Levato, H., Grosso, M., 2002, ApJ, 573, 359  
 Arenou, F., Grenon, M., Gómez, A., 1992, A&A, 258, 104  
 Auer, L. H., Mihalas, D., 1973, ApJS, 25, 433  
 Barnard, A. J., Cooper, J., Smith, E. W., 1974, JQSRT, 14, 1025  
 Claret, A., 1998, A&AS, 131, 395  
 Collins, G. W., II, Truax, R. J., 1995, ApJ, 439, 860  
 Díaz, C. G., González, J. F., Levato, H., Grosso, M., 2011, A&A, 531, A143  
 Domiciano de Souza, A., Zorec, J., Jankov, S., Vakili, F., Abe, L., Janot-Pacheco, E., 2004, A&A, 418, 781  
 Ekström, S., et al., 2012, A&A, 537, A146  
 ESA, 1997, The Hipparcos and Tycho Catalogues, ESA SP-1200, available from NASA-ADC or CDS in a machine-readable form (file name: hip\_main.dat)  
 Espinosa Lara, F., Rieutord, M., 2011, A&A, 533, A43  
 Flower, P. J., 1996, ApJ, 469, 355  
 Gigas, D., 1988, A&A, 192, 264  
 Gray D. F., 2005, The Observation and Analysis of Stellar Photospheres, 3rd ed. (Cambridge, Cambridge University Press)  
 Hauck, B., Mermilliod, M., 1998, A&AS, 129, 431  
 Hutchings, J. B., Stoeckley, T. R., 1977, PASP, 89, 19  
 Izumiura, H., 1999, in Proc. 4th East Asian Meeting on Astronomy, Observational Astrophysics in Asia and its Future ed. P. S. Chen (Kunming: Yunnan Observatory), 77  
 Jaschek, M., Egret, D., 1982, in Be Stars, Proc. IAU Symp. 98, (eds.) M. Jaschek & H.-G. Groth (Dordrecht: Reidel), p.261  
 Kurucz, R. L., 1993, Kurucz CD-ROM, No. 13, ATLAS9 Stellar Atmosphere Program and 2 km/s Grid (Cambridge: Smithsonian Astrophysical Observatory)  
 Levenhagen, R. S., 2014, ApJ, 797, 29  
 McAlister, H. A., et al., 2005, ApJ, 628, 439  
 Mihalas, D., 1972, ApJ, 177, 115  
 Napiwotzki, R., Schönberner, D., Wenske, V., 1993, A&A, 268, 653  
 Przybilla, N., Butler, K., Becker, S. R., Kudritzki, R. P., 2001, A&A, 369, 1009  
 Ruusalepp, M., 1982, in Be Stars, Proc. IAU Symp. 98, ed. M. Jaschek & H.-G. Groth (Dordrecht: Reidel), p. 303  
 Ryabchikova, T., Piskunov, N., Kurucz, R. L., Stempels, H. C., Heiter, U., Pakhomov, Yu, Barklem, P. S., 2015, Phys. Scr., 90, 054005  
 Simón-Díaz S., Herrero A., 2007, A&A, 468, 1063

- Stoeckley, T. R., 1968a, MNRAS, 140, 121  
Stoeckley, T. R., 1968b, MNRAS, 140, 141  
Stoeckley, T. R., Buscombe, W., 1987, MNRAS, 227, 801  
Stoeckley, T. R., Mihalas, D., 1973, NCAR Technical Note,  
NCAR-TN/STR-84  
Takeda, Y., 1994, PASJ, 46, 181  
Takeda, Y., 1995, PASJ, 47, 287  
Takeda, Y., Kawanomoto, S., Ohishi, N., 2008, ApJ, 678, 446  
Takeda, Y., Kambe, E., Sadakane, K., Masuda, S., 2010, PASJ,  
62, 1239  
Townsend, R. H. D., Owocki, S. P., Howarth, I. D., 2004, MNRAS,  
350, 189  
Vinicius, M.-M. F., Townsend, R. H. D., Leister, N. V., 2007, in  
Active OB Stars: Laboratories for Stellar and Circumstellar  
Physics, ASP Conf. Ser., Vol. 361, ed. S. Štefl, S. P. Owocki  
& A. T. Okazaki (San Francisco: ASP), p. 518  
Zorec, J., et al., 2011, A&A, 526, A87  
Zorec, J., et al., 2016, A&A, 595, A132  
Zorec, J., et al., 2017, A&A, 602, A83

**Table 1.** Basic parameters and observed data of program stars.

Name (1)	HR# (2)	HD# (3)	Sp.Type (4)	$V$ (5)	$T_{\text{eff}}^{\text{color}}$ (6)	$\log g^{\text{color}}$ (7)	$v_e \sin i$ (8)	$W_{4471}^{\text{He}}$ (9)	$W_{4481}^{\text{Mg}}$ (10)	$\sigma_1^{\text{He}}$ (11)	$\sigma_1^{\text{Mg}}$ (12)	$(v_e, i)$ (13)
$\zeta$ Peg	8634	214923	B8 V	3.41	11182	3.65	153	346	329	0.305	0.283	( $\sim 200$ – $250$ , $\sim 40$ – $50$ )
$\eta$ Aqr	8597	213998	B9 IV-Vn	4.03	11458	3.91	289	450	357	0.172*	0.153	( $\sim 300$ , $\sim 80$ – $90$ )
$\eta$ Tau	1165	23630	B7 III	2.87	11599	2.50	158	546	280	0.340	0.269	( $\sim 300$ – $350$ , $\sim 30$ – $35$ )
$\beta$ CMi	2845	58715	B8 Ve	2.89	11696	3.42	231	431	323	0.203	0.191	( $\sim 250$ – $300$ , $\sim 60$ – $80$ )
$\alpha$ Leo	3982	87901	B8 IVn	1.40	12223	3.54	276	511	274	0.172*	0.152	( $\sim 300$ , $\sim 80$ – $90$ )
17 Tau	1142	23302	B6 IIIe	3.70	12698	3.28	164	851	275	0.287	0.254	( $\sim 300$ , $\sim 30$ – $40$ )

(1) Star name. (2) HR number. (3) HD number. (4) Spectral type from SIMBAD. (5) Apparent visual magnitude from SIMBAD (in mag). (6) Effective temperature from  $uvby\beta$  (in K). (7) Logarithmic surface gravity from  $uvby\beta$  (in  $\text{cm s}^{-1}$ ). (8) Fitting-based projected rotational velocity (in  $\text{km s}^{-1}$ ). (9) Fitting-based equivalent width of He I 4471 (in mÅ). (10) Fitting-based equivalent width of Mg I 4481 (in mÅ). (11) First-zero frequency of He I 4471 (in  $\text{\AA}^{-1}$ ). (12) First-zero frequency of Mg II 4481 (in  $\text{\AA}^{-1}$ ). (13) Estimated solution of  $(v_e, i)$ , where  $v_e$  is in  $\text{km s}^{-1}$  and  $i$  is in degree (see Sect. 5.2 for the details).

\*Actually, an arbitrarily increased value by 10% (0.189) was used for the  $(v_e, i)$  solution search.

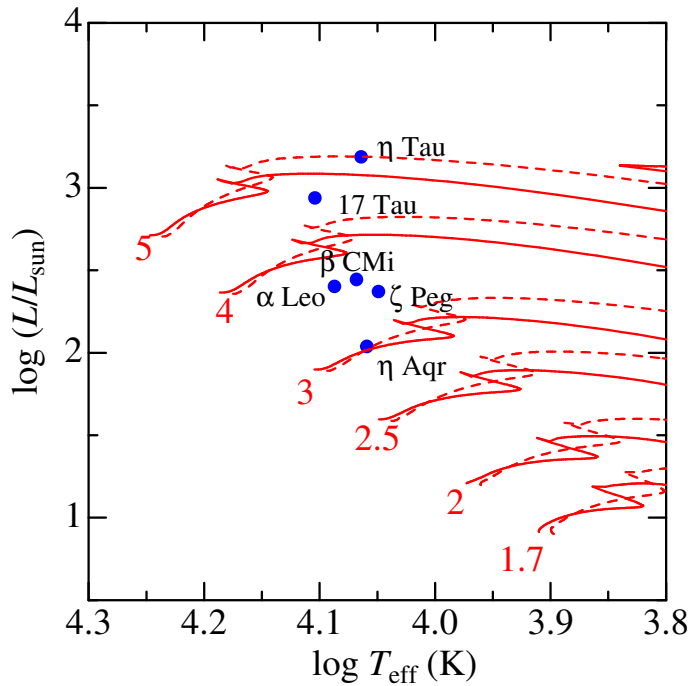


**Figure 1.** Plots of the 6 program stars on the  $\log(L/L_{\odot})$  vs.  $\log T_{\text{eff}}$  diagram, where the effective temperature ( $T_{\text{eff}}$ ) was determined from  $uvby\beta$  photometry (Sect. 2) and the bolometric luminosity ( $L$ ) was evaluated from the apparent visual magnitude (Table 1), Hipparcos parallax (ESA 1997), Arenou, Grenon & Gómez's (1992) interstellar extinction map, and Flower's (1996) bolometric correction. Theoretical evolutionary tracks corresponding to the solar metallicity computed by Ekström et al. (2012) for six different initial masses (1.7, 2, 2.5, 3, 4, and 5  $M_{\odot}$ ) are also depicted for comparison, where solid lines and dashed lines correspond to the non-rotating models and the rotating models (with 40% of the critical break-up velocity), respectively.

**Table 2.** Computed models of rotating stars and the first-zero frequencies of Fourier transforms.

Code (1)	$R_p$ (2)	$R_e$ (3)	$T_{\text{eff,p}}$ (4)	$T_{\text{eff,e}}$ (5)	$\langle T_{\text{eff}} \rangle$ (6)	$v_e \sin i$ (7)	$\sigma_1^{\text{He}}$ (8)	$\sigma_1^{\text{He}}/\sigma_1^{\text{cl}}$ (9)	$\sigma_1^{\text{Mg}}$ (10)	$\sigma_1^{\text{Mg}}/\sigma_1^{\text{cl}}$ (11)
m40r40t120v100i00	4.00	4.11	12000	11679	11854	0.0	1.938	...	2.304	...
m40r40t120v100i10					11852	17.4	2.481	0.974	2.297	0.903
m40r40t120v100i20					11844	34.2	1.308	1.011	1.287	0.997
m40r40t120v100i30					11831	50.0	0.895	1.011	0.877	0.994
m40r40t120v100i40					11815	64.3	0.712	1.034	0.682	0.993
m40r40t120v100i50					11798	76.6	0.603	1.043	0.573	0.993
m40r40t120v100i60					11781	86.6	0.535	1.047	0.505	0.991
m40r40t120v100i70					11768	94.0	0.503	1.068	0.471	1.002
m40r40t120v100i80					11759	98.5	0.479	1.065	0.444	0.991
m40r40t120v100i90					11755	100.0	0.472	1.068	0.439	0.993
m40r40t120v150i00	4.00	4.25	12000	11257	11673	0.0	3.012	...	2.304	...
m40r40t120v150i10					11667	26.0	1.688	0.993	1.702	1.004
m40r40t120v150i20					11650	51.3	0.900	1.043	0.868	1.008
m40r40t120v150i30					11622	75.0	0.634	1.075	0.592	1.006
m40r40t120v150i40					11586	96.4	0.503	1.096	0.456	0.997
m40r40t120v150i50					11546	114.9	0.424	1.100	0.384	0.999
m40r40t120v150i60					11507	129.9	0.364	1.068	0.342	1.007
m40r40t120v150i70					11473	141.0	0.344	1.096	0.310	0.989
m40r40t120v150i80					11450	147.7	0.321	1.072	0.299	0.998
m40r40t120v150i90					11442	150.0	0.315	1.068	0.292	0.991
m40r40t120v200i00	4.00	4.47	12000	10620	11421	0.0	1.938	...	2.304	...
m40r40t120v200i10					11411	34.7	1.358	1.065	1.295	1.018
m40r40t120v200i20					11383	68.4	0.723	1.117	0.661	1.023
m40r40t120v200i30					11336	100.0	0.498	1.125	0.453	1.026
m40r40t120v200i40					11274	128.6	0.393	1.143	0.347	1.011
m40r40t120v200i50					11200	153.2	0.321	1.112	0.293	1.018
m40r40t120v200i60					11123	173.2	0.285	1.115	0.255	1.000
m40r40t120v200i70					11055	187.9	0.270	1.148	0.237	1.011
m40r40t120v200i80					11007	197.0	0.258	1.147	0.225	1.002
m40r40t120v200i90					10990	200.0	0.249	1.127	0.227	1.027
m40r40t120v250i00	4.00	4.78	12000	9689	11101	0.0	3.018	...	2.299	...
m40r40t120v250i10					11089	43.4	1.156	1.134	1.057	1.039
m40r40t120v250i20					11051	85.5	0.616	1.189	0.538	1.043
m40r40t120v250i30					10986	125.0	0.425	1.199	0.367	1.038
m40r40t120v250i40					10893	160.7	0.338	1.228	0.288	1.049
m40r40t120v250i50					10775	191.5	0.279	1.206	0.237	1.029
m40r40t120v250i60					10644	216.5	0.249	1.220	0.215	1.053
m40r40t120v250i70					10520	234.9	0.231	1.229	0.195	1.038
m40r40t120v250i80					10429	246.2	0.227	1.265	0.191	1.063
m40r40t120v250i90					10395	250.0	0.219	1.238	0.182	1.032
m40r40t120v300i00	4.00	5.24	12000	8247	10730	0.0	1.932	...	2.310	...
m40r40t120v300i10					10718	52.1	1.045	1.230	0.910	1.074
m40r40t120v300i20					10682	102.6	0.566	1.312	0.456	1.060
m40r40t120v300i30					10614	150.0	0.400	1.354	0.319	1.083
m40r40t120v300i40					10506	192.8	0.314	1.367	0.243	1.061
m40r40t120v300i50					10351	229.8	0.261	1.355	0.207	1.079
m40r40t120v300i60					10155	259.8	0.238	1.396	0.182	1.070
m40r40t120v300i70					9949	281.9	0.225	1.433	0.170	1.085
m40r40t120v300i80					9787	295.4	0.227	1.515	0.164	1.098
m40r40t120v300i90					9725	300.0	0.225	1.524	0.166	1.125
m40r40t120v350i00	4.00	5.89	12000	7204	10375	0.0	1.926	...	2.316	...
m40r40t120v350i10					10370	60.8	1.016	1.395	0.830	1.142
m40r40t120v350i20					10352	119.7	0.548	1.481	0.421	1.141
m40r40t120v350i30					10316	175.0	0.387	1.532	0.286	1.132
m40r40t120v350i40					10250	225.0	0.308	1.564	0.225	1.147
m40r40t120v350i50					10126	268.1	0.255	1.544	0.197	1.193
m40r40t120v350i60					9936	303.1	0.239	1.640	0.178	1.222
m40r40t120v350i70					9705	328.9	0.234	1.737	0.164	1.219
m40r40t120v350i80					9504	344.7	0.230	1.795	0.166	1.296
m40r40t120v350i90					9422	350.0	0.236	1.870	0.166	1.319

Table 2. (Continued.)

Code (1)	$R_p$ (2)	$R_e$ (3)	$T_{\text{eff},p}$ (4)	$T_{\text{eff},e}$ (5)	$\langle T_{\text{eff}} \rangle$ (6)	$v_e \sin i$ (7)	$\sigma_1^{\text{He}}$ (8)	$\sigma_1^{\text{He}}/\sigma_1^{\text{cl}}$ (9)	$\sigma_1^{\text{Mg}}$ (10)	$\sigma_1^{\text{Mg}}/\sigma_1^{\text{cl}}$ (11)
m40r40t150v100i00	4.00	4.11	15000	14599	14816	0.0	1.932	...	2.329	...
m40r40t150v100i10					14812	17.4	2.413	0.947	2.347	0.923
m40r40t150v100i20					14802	34.2	1.241	0.959	1.281	0.992
m40r40t150v100i30					14787	50.0	0.852	0.962	0.880	0.996
m40r40t150v100i40					14768	64.3	0.675	0.981	0.684	0.996
m40r40t150v100i50					14747	76.6	0.575	0.996	0.575	0.997
m40r40t150v100i60					14727	86.6	0.504	0.987	0.507	0.995
m40r40t150v100i70					14710	94.0	0.472	1.003	0.463	0.984
m40r40t150v100i80					14699	98.5	0.443	0.986	0.446	0.995
m40r40t150v100i90					14695	100.0	0.437	0.987	0.440	0.997
m40r40t150v150i00	4.00	4.25	15000	14071	14585	0.0	1.944	...	2.329	...
m40r40t150v150i10					14578	26.0	1.602	0.943	1.690	0.997
m40r40t150v150i20					14556	51.3	0.839	0.973	0.853	0.991
m40r40t150v150i30					14523	75.0	0.593	1.005	0.585	0.994
m40r40t150v150i40					14479	96.4	0.467	1.016	0.459	1.003
m40r40t150v150i50					14431	114.9	0.393	1.021	0.386	1.004
m40r40t150v150i60					14383	129.9	0.344	1.011	0.334	0.983
m40r40t150v150i70					14342	141.0	0.320	1.018	0.310	0.991
m40r40t150v150i80					14314	147.7	0.297	0.991	0.300	1.003
m40r40t150v150i90					14304	150.0	0.291	0.986	0.292	0.993
m40r40t150v200i00	4.00	4.47	15000	13275	14262	0.0	1.944	...	2.334	...
m40r40t150v200i10					14250	34.7	1.243	0.975	1.277	1.004
m40r40t150v200i20					14215	68.4	0.657	1.016	0.648	1.004
m40r40t150v200i30					14158	100.0	0.461	1.040	0.438	0.993
m40r40t150v200i40					14082	128.6	0.357	1.036	0.341	0.992
m40r40t150v200i50					13992	153.2	0.301	1.044	0.286	0.992
m40r40t150v200i60					13899	173.2	0.260	1.018	0.257	1.008
m40r40t150v200i70					13817	187.9	0.246	1.043	0.239	1.019
m40r40t150v200i80					13760	197.0	0.231	1.030	0.226	1.010
m40r40t150v200i90					13740	200.0	0.233	1.055	0.219	0.990
m40r40t150v250i00	4.00	4.78	15000	12111	13847	0.0	1.944	...	2.323	...
m40r40t150v250i10					13832	43.4	1.012	0.992	1.025	1.008
m40r40t150v250i20					13785	85.5	0.557	1.077	0.518	1.003
m40r40t150v250i30					13705	125.0	0.376	1.061	0.353	0.999
m40r40t150v250i40					13590	160.7	0.290	1.055	0.273	0.995
m40r40t150v250i50					13447	191.5	0.252	1.091	0.231	1.002
m40r40t150v250i60					13288	216.5	0.218	1.067	0.208	1.020
m40r40t150v250i70					13139	234.9	0.209	1.110	0.188	1.000
m40r40t150v250i80					13031	246.2	0.194	1.079	0.183	1.019
m40r40t150v250i90					12992	250.0	0.194	1.097	0.185	1.045
m40r40t150v300i00	4.00	5.24	15000	10309	13347	0.0	1.938	...	2.328	...
m40r40t150v300i10					13332	52.1	0.906	1.067	0.865	1.021
m40r40t150v300i20					13284	102.6	0.492	1.140	0.439	1.020
m40r40t150v300i30					13196	150.0	0.333	1.129	0.298	1.011
m40r40t150v300i40					13057	192.8	0.260	1.134	0.239	1.045
m40r40t150v300i50					12860	229.8	0.225	1.167	0.203	1.054
m40r40t150v300i60					12618	259.8	0.200	1.174	0.176	1.036
m40r40t150v300i70					12370	281.9	0.188	1.197	0.164	1.046
m40r40t150v300i80					12180	295.4	0.191	1.273	0.158	1.057
m40r40t150v300i90					12108	300.0	0.182	1.232	0.160	1.084
m40r40t150v350i00	4.00	5.89	15000	7384	12835	0.0	1.938	...	2.328	...
m40r40t150v350i10					12828	60.8	0.876	1.203	0.780	1.074
m40r40t150v350i20					12807	119.7	0.467	1.264	0.396	1.075
m40r40t150v350i30					12766	175.0	0.326	1.290	0.276	1.093
m40r40t150v350i40					12683	225.0	0.258	1.314	0.213	1.084
m40r40t150v350i50					12517	268.1	0.221	1.342	0.182	1.106
m40r40t150v350i60					12264	303.1	0.203	1.389	0.172	1.183
m40r40t150v350i70					11964	328.9	0.197	1.465	0.158	1.175
m40r40t150v350i80					11710	344.7	0.193	1.505	0.160	1.249
m40r40t150v350i90					11608	350.0	0.193	1.530	0.151	1.199

(1) Model code (m\*\*r\*\*t\*\*\*v\*\*\*i\*\*), which describes the adopted stellar mass ( $M$ ), polar radius ( $R_p$ ), polar effective temperature ( $T_{\text{eff},p}$ ), equatorial rotation velocity ( $v_e$ ), and inclination angle ( $i$ ). For example, "m40r40t150v300i30" is the case of  $M = 4.0M_\odot$ ,  $R_p = 4.0R_\odot$ ,  $T_{\text{eff},p} = 15000$  K,  $v_e = 300$  km s $^{-1}$ , and  $i = 30^\circ$ . (2) Polar radius (in  $R_\odot$ ). (3) Equatorial radius (in  $R_\odot$ ). (4) Polar effective temperature (in K). (5) Equatorial effective temperature (in K). (6) Mean effective temperature in K (which was derived by averaging the local effective temperature over the observed stellar disk while weighting according to the local continuum intensity). (7) Product of  $v_e$  and  $\sin i$  (in km s $^{-1}$ ). (8) First-zero frequency of He 4471 (in  $\text{\AA}^{-1}$ ). (9) Ratio of  $\sigma_1^{\text{He}}$  to  $\sigma_1^{\text{cl}}$ , where  $\sigma_1^{\text{cl}}$  is the first-zero frequency of classical rotational broadening function (see, e.g., Gray 2005), which is related to  $v_e \sin i$  as  $\sigma_1^{\text{cl}} = 0.660/(\lambda v_e \sin i/c)$  ( $\lambda$ : wavelength,  $c$ : velocity of light). (10) First-zero frequency of Mg 4481 (in  $\text{\AA}^{-1}$ ). (11) Ratio of  $\sigma_1^{\text{Mg}}$  to  $\sigma_1^{\text{cl}}$ .

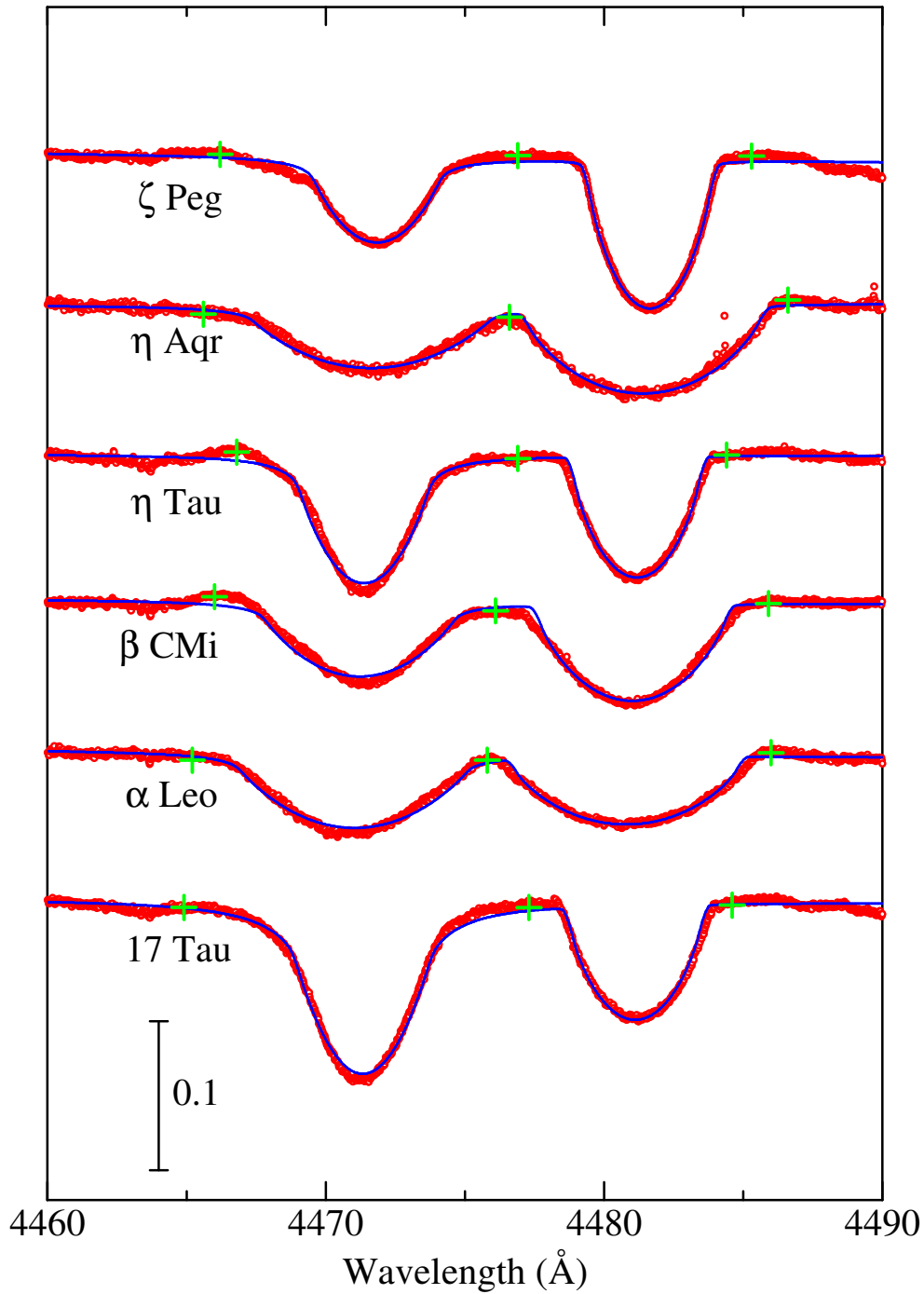


**Figure 2.** Synthetic spectrum fitting in the 4460–4490  $\text{\AA}$  region comprising He I 4471 and Mg II 4481 lines, which was accomplished based on the conventional modeling (using the plane-parallel model atmosphere and the classical rotational broadening function) by adjusting four parameters [ $A(\text{He})$ ,  $A(\text{Mg})$ ,  $v_e \sin i$ ,  $\Delta\lambda$ ; cf. Sect. 3.2]. The observed data are plotted by red symbols, while the best-fit theoretical spectra are shown by blue solid lines. The spectra are arranged (from top to bottom) in the ascending order of  $T_{\text{eff}}$  as in Table 1, and a vertical offset of 0.1 is applied to each spectrum relative to the adjacent one. The green crosses indicate the reference points of pseudo-continuum (cf. Sect. 4.1), based on which the normalized line-depth profiles (to be used for calculating the Fourier transforms) were computed.

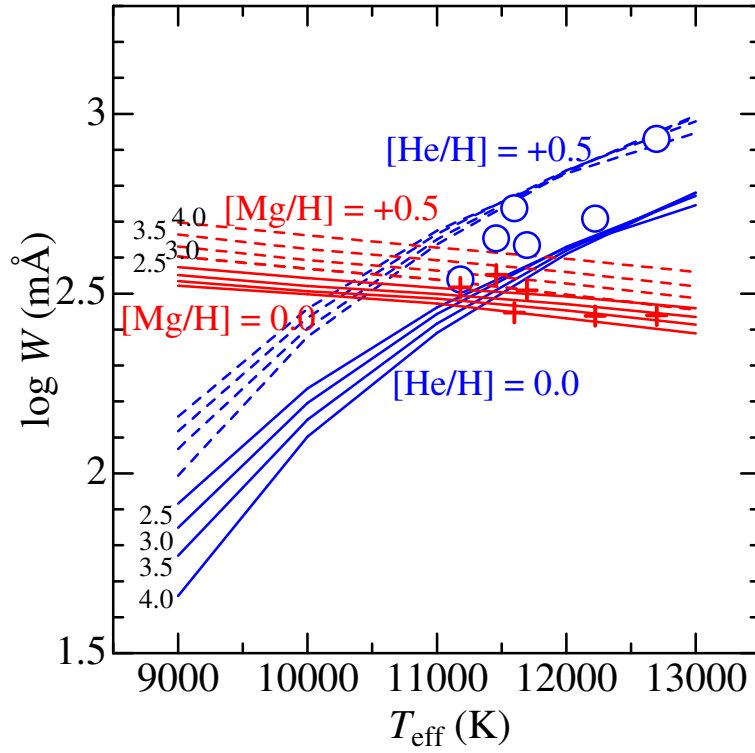


**Figure 3.** Equivalent widths ( $W$ ) of He I 4471 (blue) and Mg II (red) plotted against the effective temperature. The theoretical  $W$  values (computed for models with  $T_{\text{eff}} = 9000, 10000, 11000, 12000,$  and  $13000$  K, and  $\log g = 2.5, 3.0, 3.5,$  and  $4.0$ ) are depicted by lines (solid lines: solar abundance, dashed lines: overabundance by  $+0.5$  dex), while the observed values for 6 program stars are shown by symbols (open circles for He 4471 and crosses for Mg 4481). Note the markedly large dependence of  $W(\text{He})$  upon  $T_{\text{eff}}$  (increasing with  $T_{\text{eff}}$ ), while  $W(\text{Mg})$  is only weakly  $T_{\text{eff}}$ -dependent (decreasing with  $T_{\text{eff}}$ ). Regarding the gravity dependence,  $W(\text{He})$  tends to decrease with an increase in  $\log g$  (indicated in the figure), while the tendency is reversed for  $W(\text{Mg})$ .

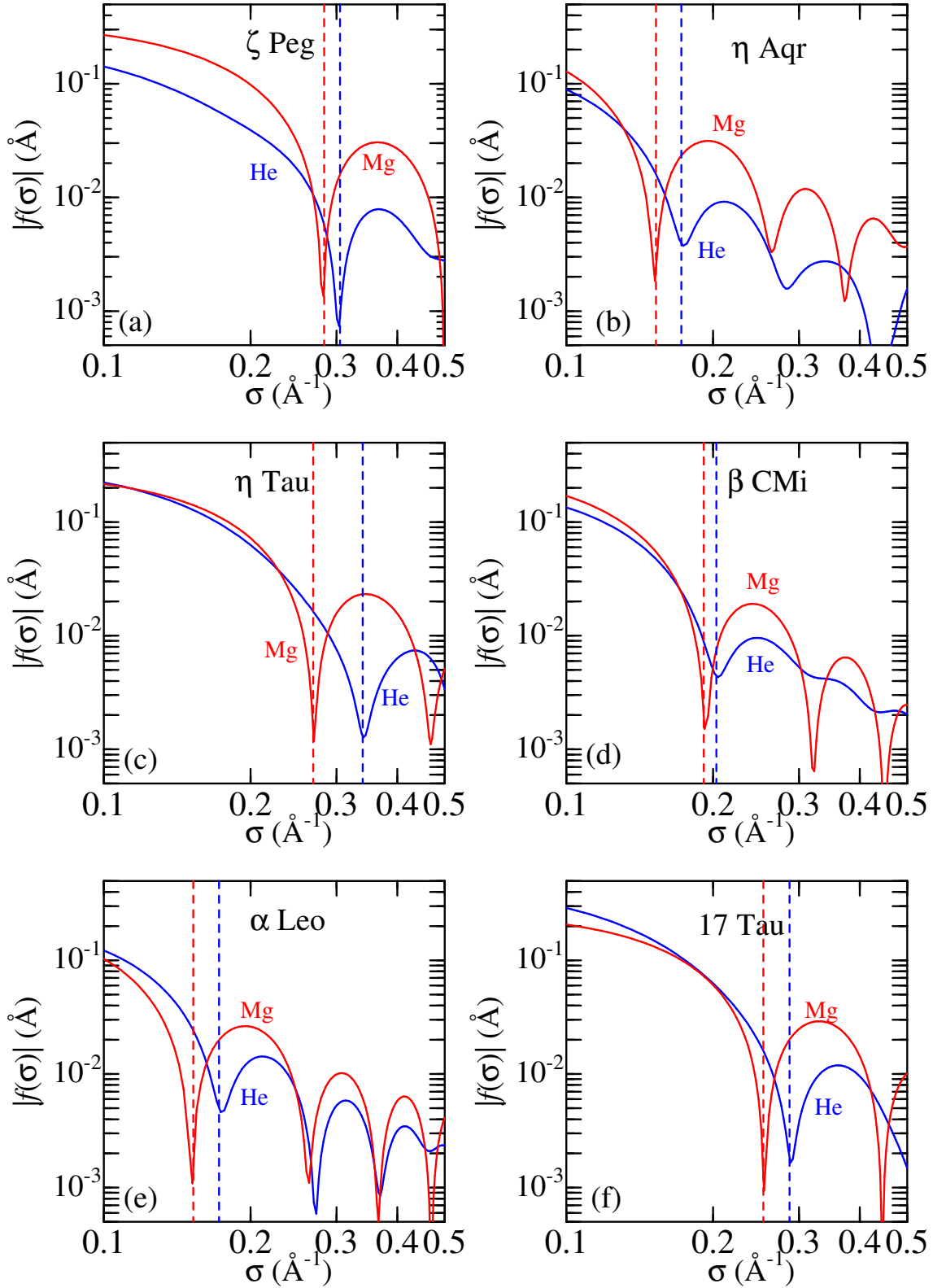


**Figure 4.** Fourier transform amplitudes  $[|f(\sigma)|]$  plotted against  $\sigma$ , for the observed profiles of He 4471 (blue) and Mg 4481 (red). The positions of the first zero ( $\sigma_1$ ) are indicated by vertical dashed lines. (a)  $\zeta$  Peg, (b)  $\eta$  Aqr, (c)  $\eta$  Tau, (d)  $\beta$  CMi, (e)  $\alpha$  Leo, and (e) 17 Tau.

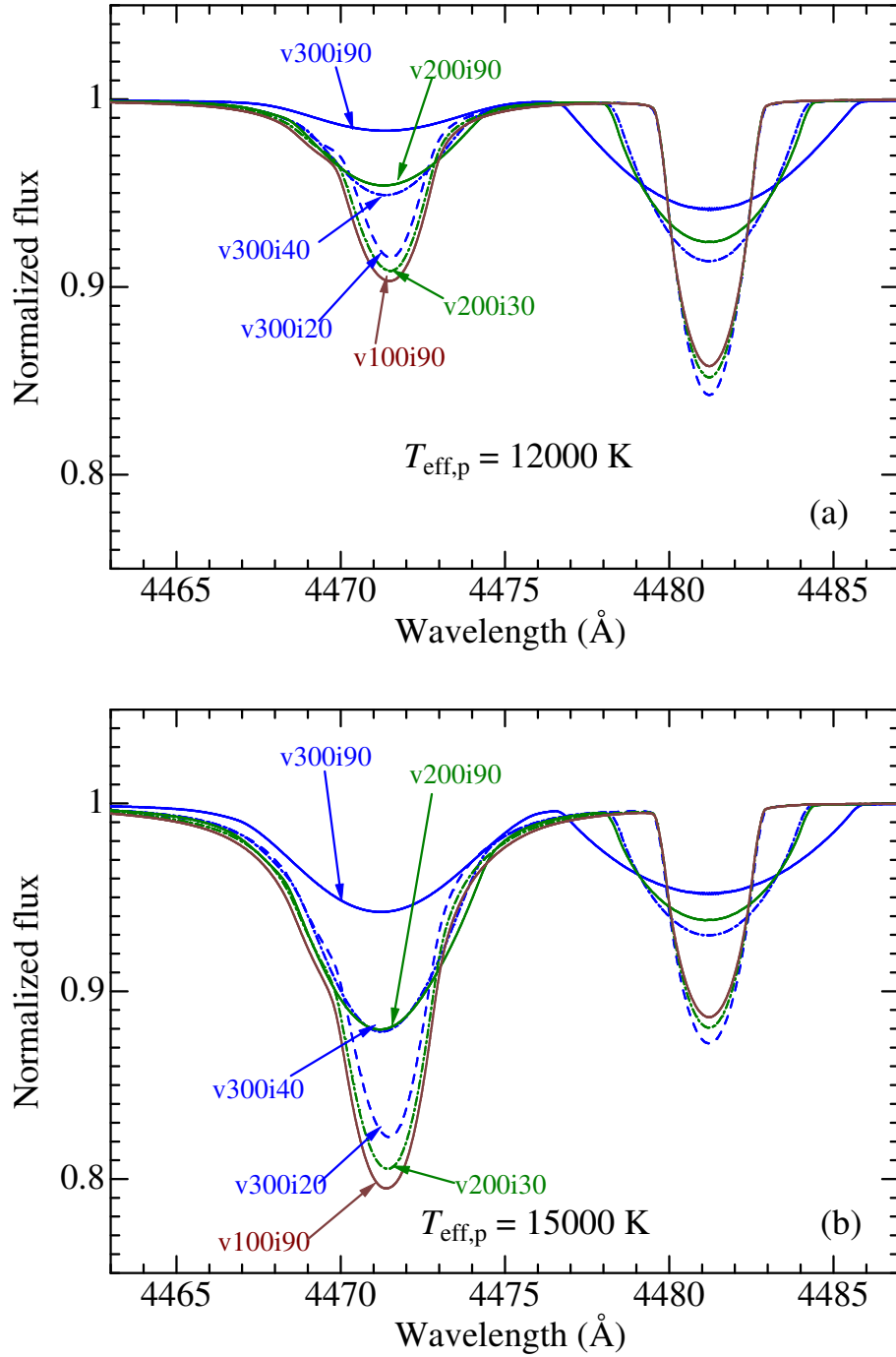


**Figure 5.** Theoretically synthesized spectra in the 4463–4487 Å region computed for six representative models of v100i90, v200i30, v200i90, v300i20, v300i40, and v300i90 (the code “v\*\*\*i\*\*” means  $v_e = *** \text{ km s}^{-1}$  and  $i = **^\circ$ ), which were so chosen as to demonstrate the three  $v_e \sin i$  cases of  $\sim 100$ ,  $\sim 200$ , and  $300 \text{ km s}^{-1}$ . The results for  $v_e = 100$ , 200, and  $300 \text{ km s}^{-1}$  are depicted in brown, green, and blue, respectively. The upper panel (a) shows the case for  $T_{\text{eff,p}} = 12000 \text{ K}$ , while the lower panel (b) is for  $T_{\text{eff,p}} = 15000 \text{ K}$ .

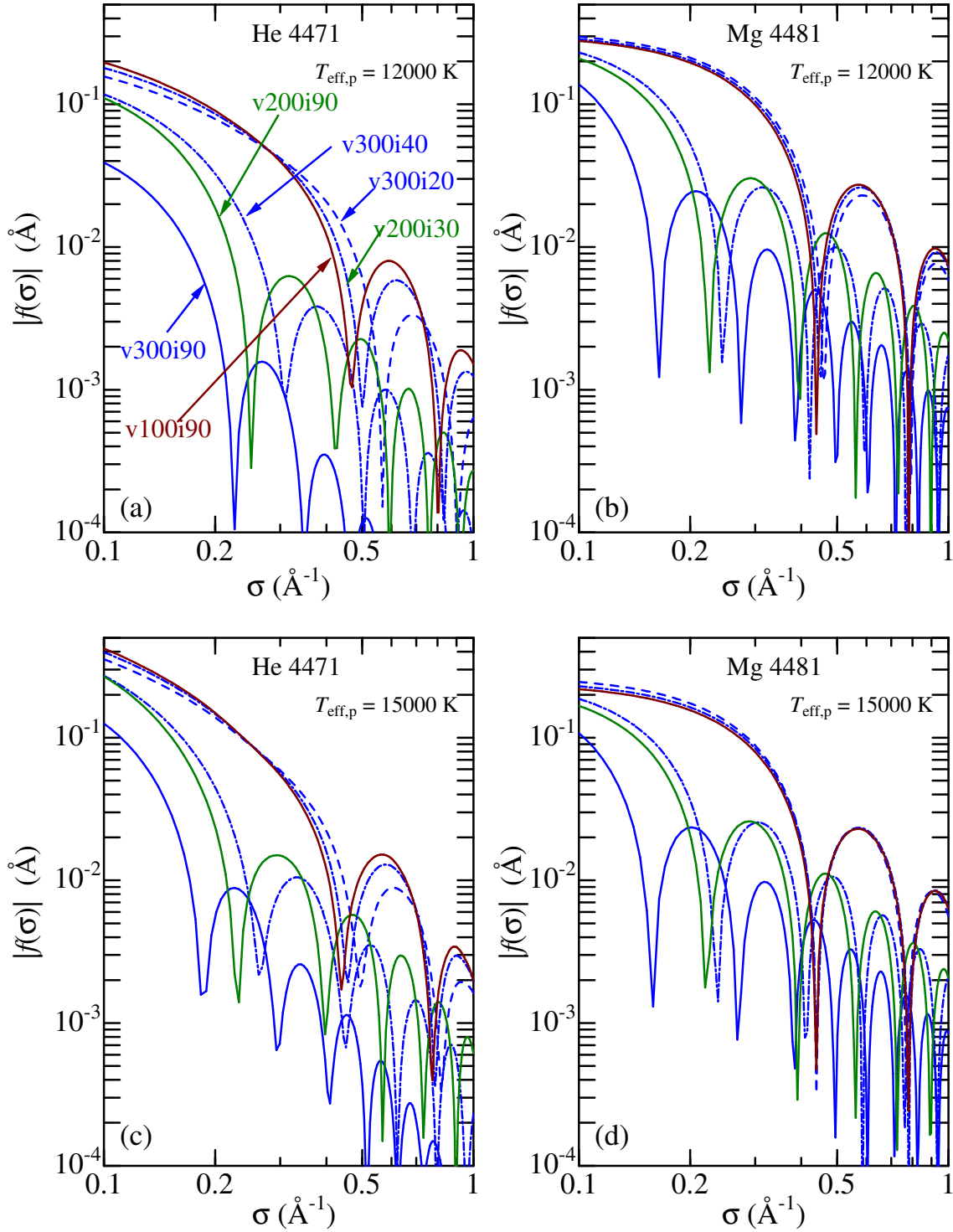


**Figure 6.** Fourier transform amplitudes  $[|f(\sigma)|]$  plotted against  $\sigma$ , for the theoretical profiles of He 4471 (left panels) and Mg 4481 (right panels) computed for six representative models (same as those shown in Fig. 5). The upper panels (a) and (b) show the results for  $T_{\text{eff,p}} = 12000$  K, while the lower panels (c) and (d) are for  $T_{\text{eff,p}} = 15000$  K.

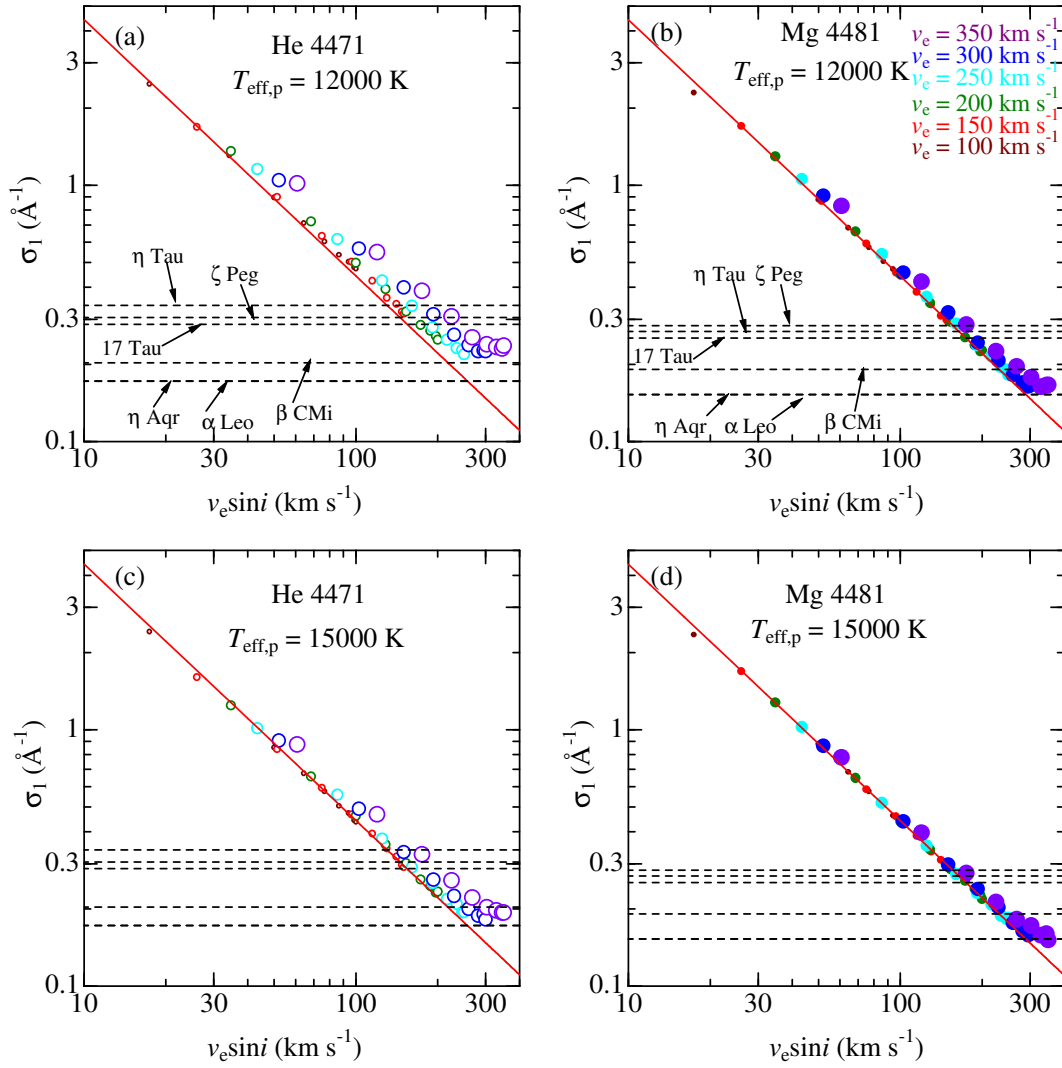


**Figure 7.** The values of theoretical  $\sigma_1$ , measured from the Fourier transforms of simulated spectra for gravity-darkened models, are plotted against  $v_e \sin i$ . The results for He 4471 (left panels) and Mg 4481 (right panels) are shown in open and filled circles, respectively, where those corresponding to different  $v_e$  are discriminated by their size and color (larger symbol for higher  $v_e$ ). The solid line shows the classical relation  $\sigma_1 = 0.660 / (\lambda v_e \sin i / c)$ . The observed  $\sigma_1$  values for each of the six program stars are indicated by horizontal dashed lines. The upper panels (a) and (b) show the results for  $T_{\text{eff,p}} = 12000$  K, while the lower panels (c) and (d) are for  $T_{\text{eff,p}} = 15000$  K.

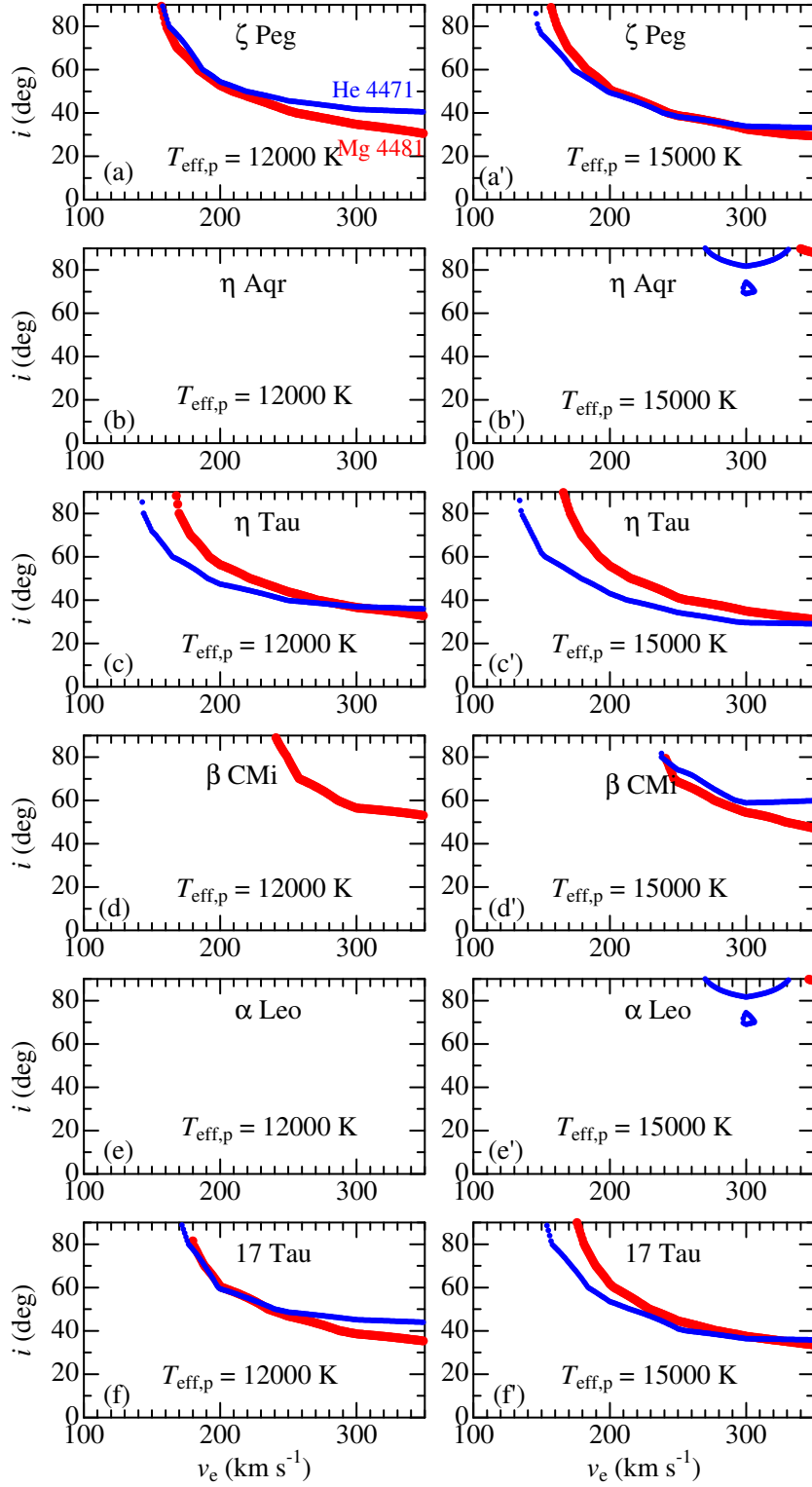


**Figure 8.** Graphical display of contours in the  $(v_e, i)$  plane, which were derived as the solution satisfying the equation  $\sigma_1^{\text{obs}} = \sigma_1^{\text{th}}(i, v_e)$ . The results for He 4471 and Mg 4481 are shown in thinner blue traces and thicker red traces, respectively. From top to bottom are arranged the panels for  $\zeta$  Peg,  $\eta$  Aqr,  $\eta$  Tau,  $\beta$  CMi,  $\alpha$  Leo, and 17 Tau, where each of the left-hand and right-hand panels are for  $T_{\text{eff,p}} = 12000$  K and  $T_{\text{eff,p}} = 15000$  K, respectively. Note that, in deriving the results for  $\eta$  Aqr and  $\alpha$  Leo, the observed  $\sigma_1^{\text{He}}$  values for He 4471 were arbitrarily increased by 10%, in order to bring the solution to a determinable level.